Heliyon 10 (2024) e30923

Contents lists available at ScienceDirect

Heliyon

journal homepage: www.cell.com/heliyon

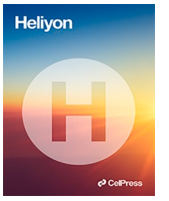

Research article

Spatial calibration and uncertainty reduction of the SWAT model using multiple remotely sensed data

Sangchul Lee [a,*], Dongho Kim [b], Gregory W. McCarty [c], Martha Anderson [c], Feng Gao [c], Fangni Lei [c], Glenn E. Moglen [d], Xuesong Zhang [c], Haw Yen [e], Junyu Qi [f], Wade Crow [c], In-Young Yeo [g], Liang Sun [h]

[a] *Division of Environmental Science & Ecological Engineering, College of Life Sciences & Biotechnology, Korea University, Seoul 02841, Republic of Korea*
[b] *Department of Environmental Engineering, University of Seoul, Dongdaemun-gu, Seoul 02504, Republic of Korea*
[c] *USDA-ARS, Hydrology and Remote Sensing Laboratory, Beltsville, MD 20705, USA*
[d] *Department of Civil and Environmental Engineering, The University of North Carolina at Charlotte, Charlotte, NC 28223, USA*
[e] *School of Forestry and Wildlife Sciences, Auburn University, Auburn, AL 36849, USA*
[f] *Earth System Science Interdisciplinary Center, University of Maryland, College Park, 5825 University Research Ct, College Park, MD 20740, USA*
[g] *School of Engineering, The University of Newcastle, Callaghan NSW 2308, Australia*
[h] *Key Laboratory of Agricultural Remote Sensing, Ministry of Agriculture / Institute of Agricultural Resources and Regional Planning, Chinese Academy of Agricultural Sciences, Beijing 100081, China*

A R T I C L E I N F O

Keywords:
Remotely sensed products
Additional constraints
Parameter uncertainty
Soil and water assessment tool (SWAT)

A B S T R A C T

Remotely sensed products are often used in watershed modeling as additional constraints to improve model predictions and reduce model uncertainty. Remotely sensed products also enabled the spatial evaluation of model simulations due to their spatial and temporal coverage. However, their usability is not extensively explored in various regions. This study evaluates the effectiveness of incorporating remotely sensed evapotranspiration (RS-ET) and leaf area index (RS-LAI) products to enhance watershed modeling predictions. The objectives include reducing parameter uncertainty at the watershed scale and refining the model's capability to predict the spatial distribution of ET and LAI at sub-watershed scale. Using the Soil and Water Assessment Tool (SWAT) model, a systematic calibration procedure was applied. Initially, solely streamflow data was employed as a constraint, gradually incorporating RS-ET and RS-LAI thereafter. The results showed that while 14 parameter sets exhibit satisfactory performance for streamflow and RS-ET, this number diminishes to six with the inclusion of RS-LAI as an additional constraint. Furthermore, among these six sets, only three effectively captured the spatial patterns of ET and LAI at the sub-watershed level. Our findings showed that leveraging multiple remotely sensed products has the potential to diminish parameter uncertainty and increase the credibility of intra-watershed process simulations. These results contributed to broadening the applicability of remotely sensed products in watershed modeling, enhancing their usefulness in this field.

* Corresponding author.
E-mail address: sangchul.lee84@gmail.com (S. Lee).

https://doi.org/10.1016/j.heliyon.2024.e30923
Received 17 July 2023; Received in revised form 4 May 2024; Accepted 8 May 2024
Available online 9 May 2024

1. Introduction

Uncertainty remains a central issue in hydrologic modeling. Despite the validation processes conducted during calibration, uncertainty always persists [1]. A notable source of this uncertainty lies in the insufficiency of observations. In the field of hydrologic modeling, observations are commonly constrained to water quantity and/or quality measurements obtained at the outlet of the study site [1]. To reduce the predictive uncertainty stemming from data paucity, the integration of soft data—such as expert insights, literature surveys, remotely sensed data, and extensive field monitoring—have been suggested [2–5]. Soft data serve to well depict intra-watershed processes, hydrologic phenomena occurring between streams and upland areas [6]. Their inclusion has demonstrated efficacy in constraining model parameter values, attenuating predictive uncertainty [5,7,8].

The Soil and Water Assessment Tool (SWAT) model, one of semi-distributed hydrologic models, commonly encounters predictive uncertainty owing to limited observational data [9]. One remedy to address this challenge involves the incorporation of remotely sensed products into SWAT simulations, such as plant growth dynamics [10], wetland hydrologic patterns [5,11], and soil moisture [12]. Remotely sensed products offer advantages over in-situ measurements by providing broad-scale observations for prolonged durations, which mitigates concerns regarding data scarcity for hydrologic modeling operations [13]. The SWAT model calibrated against remotely sensed evapotranspiration (referred to as RS-ET) products showed enhanced model performances [14–17]. Evapotranspiration (ET), encompassing the combined fluxes of evaporation and transpiration, holds importance in water and energy cycling. Consequently, improved ET predictions could contribute to the enhanced reliability of the model.

RS-ET products are frequently combined with streamflow data to find optimal hydrologic parameter values during model calibration [14–19]. The concurrent utilization of streamflow and RS-ET products has been shown to effectively constrain parameter values and decrease parameter uncertainty [14–18]. Wambura, 2018 [14] illustrated the utility of RS-ET products in mitigating equifinality, which refers to the tendency for parameter sets to yield equally satisfactory model outcomes [20]. Furthermore, a study conducted by Rajib, (2020) [21] revealed enhancements in modeled ET predictions through the incorporation of vegetation parameters and the integration of RS-ET products for evaluating ET variations across a landscape. This was confirmed by an improvement in the model performance measure, the Kling-Gupta Efficiency (KGE), from 0.6 to 0.7 [21].

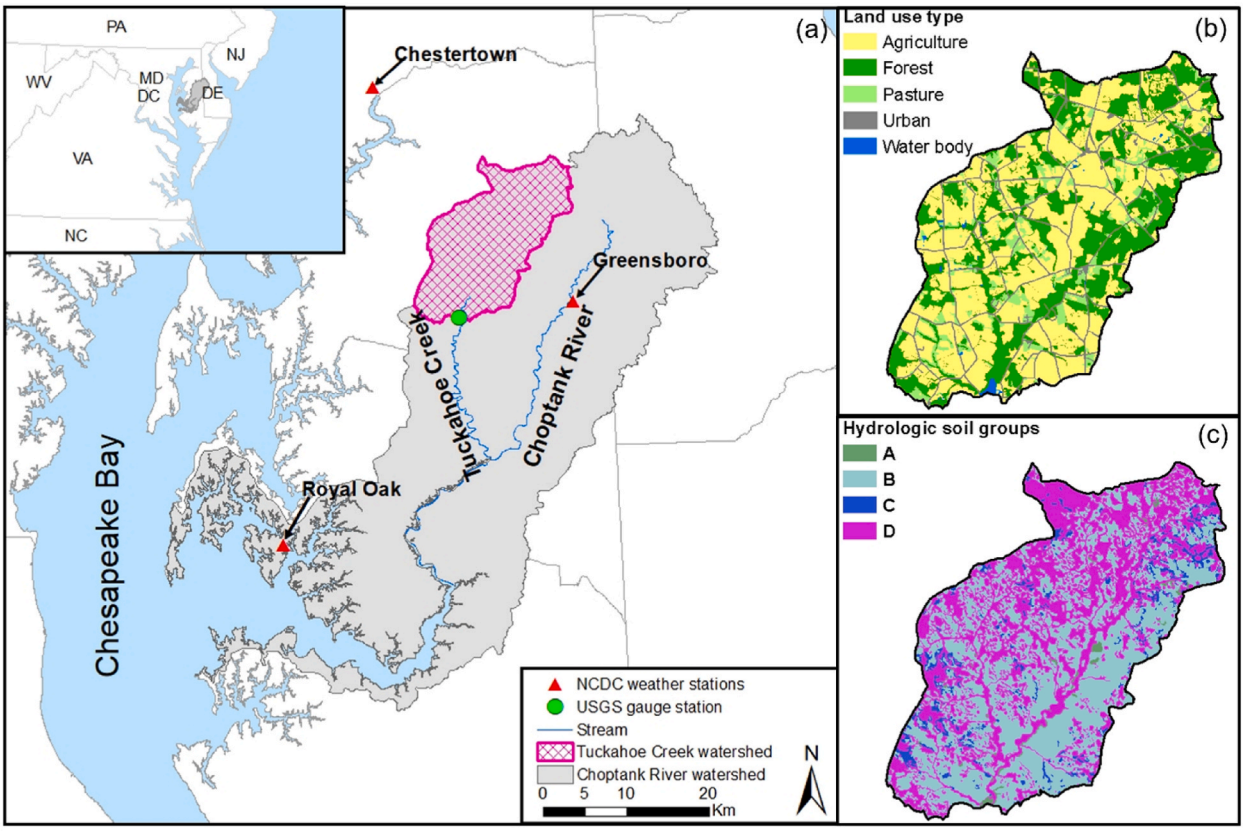

Fig. 1. (a) Geographical location, (b) land use composition, and (c) distribution of hydrologic soil groups of the study area (adapted from Lee, 2018 [32])) Note: hydrologic soil groups (HSGs) are classified based on their infiltration rates as follows: Type A – well-drained soils with a water infiltration rate of 7.6–11.4 mm h^{-1}; Type B – moderately well-drained soils with a rate of 3.8–7.6 mm h^{-1}; Type C – moderately poorly-drained soils with a rate of 1.3–3.8 mm h^{-1}; and Type D – poorly-drained soils with a rate of 0–1.3 mm h^{-1} [33]. The distribution of HSGs within the TCW is as follows: HSG–A, HSG–B, HSG–C, and HSG–D account for 0.3 %, 55.8 %, 2.2 %, and 41.7 % of the watershed, respectively.

With the enhanced availability of remotely sensed leaf area index (RS-LAI) products, hydrological modeling studies actively adopt these data [22,23]. Leaf area index (LAI) measures the number of leaves over a certain area of land and is important for understanding how plants transpire water [24,25]. Water taken up by roots and released through plant leaves as vapor makes up a substantial part of total evapotranspiration (ET) in vegetated areas. As a result, many studies have shown a strong connection between ET and LAI [26]. In compliance with previous studies, the use of both RS-ET and RS-LAI was shown to reduce model uncertainty to enable spatial assessment [27]. However, their benefits are not well explored in various areas. Since the performance of watershed models spatio-temporally varies [28,29], it is necessary to test the impacts of RS-ET and RS-LAI uses in various regions.

The main objective of this study is to investigate how two remotely sensed datasets, RS-ET and RS-LAI, could improve hydrologic modeling at the watershed level. This study used daily remotely sensed products to provide new insight on the use of high-temporal remotely sensed products, given that temporally coarse remotely sensed products have been commonly applied in previous studies [10, 14,15,27]. The selected hydrologic model for this study was SWAT (2012 version), primarily due to its extensive integration of remotely sensed products. To accomplish the research objective, the study employed a lumped parameterization approach at the watershed level, incorporating three constraints (i.e., streamflow, RS-ET, and RS-LAI). For comparative analyses with previous studies, a commonly used parameterization method for SWAT calibration/validation (i.e., lumped parameterization) was selected in this study. Since the use of either RS-ET or RS-LAI with SWAT has been widely conducted, this study performed the simultaneous use of RS-ET and RS-LAI for SWAT. The parameter sets (referred to as PARs hereafter) yielding satisfactory streamflow and ET simulations (referred to as "PARs-1″) were selected from the entire set of PARs investigated during calibration. Furthermore, PARs exhibiting satisfactory model performance measures for streamflow, ET, and LAI (referred to as "PARs-2″) were identified from the explored PARs. Specifically, this study aimed to: (i) compare PARs-1 and PARs-2 along with their simulated outputs (e.g., streamflow, ET, and LAI), and investigate the influence of RS-ET and RS-LAI in constraining satisfactory PARs; and (ii) to assess utility of RS-ET and RS-LAI products as additional constraints in identifying PARs that accurately capture the spatial distribution of ET and LAI.

2. Materials and methods

2.1. Study site

This research was carried out within the Tuckahoe Creek watershed (TCW, 220 km^2), located upstream of the gauge station #01491500 operated by the U.S. Geological Survey (USGS) (Fig. 1a). Positioned as a sub-basin within the Choptank River watershed, situated in the coastal plain of the Chesapeake Bay Watershed (CBW), the TCW has been a subject of comprehensive research led by the U.S. Department of Agriculture-Natural Resources Conservation Service (USDA-NRCS) [30] and the USDA-Agricultural Research Service (USDA-ARS) [31]. The land cover within the TCW is predominantly comprised of croplands (54 %), followed by forest (32.8 %), pasture (8.4 %), urban areas (4.2 %), and water bodies (0.6 %). Primary crops cultivated in the watershed include corn, soybeans, and winter wheat. Soil composition, as classified by the USDA-NRCS, predominantly consists of moderately well-drained (Hydrologic Soil Group (HSG) – B, 55.8 %) and poorly drained soils (HSG – D, 41.7 %) (Fig. 1c).

According to long-term observations from three meteorological stations operated by the National Oceanic Atmospheric Administration (NOAA)'s National Climate Data Center (NCDC), the annual mean precipitation and daily average temperature are estimated to be 1166 mm (±228 mm) and 13 °C (±1 °C), respectively, over the past three decades (1985–2014). The TCW experiences a humid subtropical climate, influenced by the Chesapeake Bay and the Atlantic Ocean, resulting in relatively uniform precipitation throughout the year. Characterized by flat topography (ranging from 0 to 32 m above sea level), the region has experienced a substantial increase in irrigation practices, particularly for corn and soybean cultivation during the summer season, which exacerbates water loss through ET [34]. The water balance dynamics in this area are notably influenced by seasonal fluctuations in ET. Consequently, accurate simulations of ET and LAI are critical for improving predictions generated by hydrological models within this region.

2.2. Soil and Water Assessment Tool

The Soil and Water Assessment Tool (SWAT) model is a watershed-scale model specifically aimed to investigate the impacts of both natural environmental factors and human activities on hydrological processes within agricultural watersheds [33]. Comprising various components, SWAT includes components for climate, hydrology, nutrient and pesticide dynamics, erosion, land cover and vegetation, agricultural management practices, and channel processes [33]. In its operation, the model divides a given watershed into sub-watersheds and further delineates hydrological response units (HRUs). Each HRU represents a distinct combination of land use, soil type, and slope characteristics within individual sub-watersheds. At this level, hydrologic variables are computed independently for each HRU, with subsequent aggregation of outputs occurring at both the sub-watershed and watershed levels through channel processes [33]. The water balance for each HRU is calculated using Eq. (1):

$$SW_t = SW_0 + \sum_{i=1}^{t} \left(R_{day} - Q_{surf} - E_a - W_{seep} - Q_{gw}\right) \quad (1)$$

Where, SW_t is the final soil water content (mm H_2O), SW_0 is the initial soil water content (mm H_2O), t is the time (days), R_{day} is the amount of precipitation on day i (mm H_2O), Q_{surf} is the amount of surface runoff on day i (mm H_2O), E_a is the amount of ET on day i (mm H_2O), W_{seep} is the amount of percolation and bypass flow at the bottom of the soil profile on day i (mm H_2O), and Q_{gw} is the amount of return flow on day i (mm H_2O). Within the SWAT model, the calculation of surface runoff volume is accomplished through

either a modified Soil Conservation Service (SCS) curve number method or the Green and Ampt infiltration approach. This study employed the modified SCS curve number method.

The SWAT model initiates by computing potential evapotranspiration (PET) and then subsequently estimates actual evapotranspiration (AET). Within the SWAT model, three methods for calculating potential evapotranspiration (PET) are available: Penman–Monteith, Priestley–Taylor, and Hargreaves. Following the computation of PET, the estimation of AET involves accounting for evaporation from the canopy, soil evaporation, and plant transpiration, with the specific calculations dependent on the chosen PET method [33]. The quantification of actual soil evaporation is determined based on soil depth and soil water content, while actual plant transpiration is computed by adjusting optimal plant transpiration rates to account for limited soil water availability.

In this study, the Penman–Monteith method, represented by Eq. (2), was utilized for PET calculation:

$$\lambda E = \frac{\Delta \bullet (H_{net} - G) + \rho_{air} \bullet c_p \bullet \left[e_z^0 - e_z\right]/r_a}{\Delta + \gamma \bullet (1 + r_c/r_a)} \quad (2)$$

Where, λ E is the latent heat of vaporization (MJ kg^{-1}), E the depth rate evaporation (mm d^{-1}), Δ the slope of the saturation vapor pressure-temperature curve (kPa $\circ C^{-1}$), H_{net} the net radiation (MJ m^{-2} d^{-1}), G the ground heat flux density (MJ m^{-2} d^{-1}), ρ_{air} the air density (kg m^{-3}), c_p the specific heat at constant pressure (MJ kg^{-1} $\circ C^{-1}$), e_z^0 the saturation vapor pressure of air at height z (kPa), e_z the water vapor pressure of air at height z (kPa), γ the psychrometric constant (kPa $\circ C^{-1}$), r_c the plant canopy resistance (s m^{-1}) and r_a the diffusion resistance of the air layer (aerodynamic resistance) (s m^{-1}).

Within the SWAT model, dynamic leaf area index (LAI) estimates are derived as a function of the optimal leaf area development curve, which governs LAI growth based on accumulated potential heat units. These units are calculated daily as the difference between the daily average temperature and the base temperature, whereby the base temperature represents the minimum threshold for vegetation growth and is typically set to 0 °C by default. When the daily average temperature falls below the base temperature, the daily heat unit is set as zero. During the initial growth phase, leaf area development is simulated according to the prescribed optimal leaf area development curve, as defined by Eq. (3).

$$fr_{LAImx} = \frac{fr_{PHU}}{fr_{PHU} + exp\left(\curlyvee_1 - \curlyvee_2 \bullet fr_{PHU}\right)} \quad (3)$$

Where, fr_{LAImx} is the fraction of the plant's maximum leaf area index corresponding to a given fraction of potential heat units for the plan, fr_{PHU} is the fraction of potential heat units accumulated for the plant on a given day in the growing season, and $\curlyvee_1$ and $\curlyvee_2$ are the shape coefficients. In the leaf area development curve, once the LAI attains its maximum value, which is specific to the vegetation type, this maximum LAI is sustained until the onset of leaf senescence. Subsequently, there is a linear decline in LAI before dormancy [33].

2.3. Input and calibration data

Climate and geospatial data are needed for the SWAT simulations (Table 1). Daily records of precipitation and temperature spanning from 2008 to 2014 were acquired from NOAA NCDC monitoring stations (Fig. 1a). Solar radiation, relative humidity, and wind speed data on a daily basis were generated using the SWAT model's internal weather generator [33], owing to the absence of observations for these climatic variables in the monitoring station within the region. The monitoring station in Greensboro solely provided daily precipitation data; hence, daily temperature records were derived from the nearest station in Chestertown from January 2008 to May 2011. Given that temperature data ceased to be collected at the Chestertown station after May 2011, data from the third nearest station in Royal Oak were utilized for the period spanning June 2011 to December 2014. Further details regarding the calculation of daily solar radiation, relative humidity, and wind speed via the weather generator are outlined in Text S1 of the Supplementary Material.

Table 1
Input and calibration data for the SWAT model.

Data Type	Source	Description	Year
DEM	MD-DNR	LiDAR-based 10-m resolution	2006
Land Use	USDA-NASS	Cropland Data Layer (CDL)	2008–2012
	MRLC	National Land Cover Database (NLCD)	2006
	USDA-FSA-APFO	National Agricultural Imagery Program digital Orthophoto quad imagery	1998
	US Census Bureau	TIGER road map	2010
Soils	USDA-NRCS	Soil Survey Geographical Database (SSURGO)	2012
Climate	NCDC	Daily precipitation and temperature	2008–2014
Streamflow	USGS	Daily streamflow	2008–2014
RS-ET	Sun, 2017 [35]	Daily ET (30-m spatial resolution)	2010–2014
RS-LAI	NASA	Daily LAI (500-m spatial resolution)	2010–2014
	USDA-ARS		

MRLC: Multi-Resolution Land Characteristics Consortium, USDA-FSA-APFO: USDA-Farm Service Agency-Aerial Photography Field Office, and TIGER: Topologically Integrated Geographic Encoding and Referencing. Detailed values (average, minimum and maximum) of precipitation, temperature, streamflow, RS-ET and RS–LAI are available in Table S2 of the Supplementary Material.

Digital elevation model (DEM) data were sourced from the Maryland Department of Natural Resources (MD-DNR) and were post-processed to a 10-m resolution through nearest-neighbor interpolation conducted by USDA-ARS, Beltsville. This post-processing was undertaken to mitigate the potential distortion of slope values resulting from finer or coarser spatial resolutions of the DEM [36]. Soil map data pertinent to the study area were obtained from the Soil Survey Geographical Database (SSURGO). Additionally, a land use map developed by Lee (2016) [37], derived from various geospatial sources as detailed in Table 1 [37], was employed. This map encompasses eight distinct crop rotations (Table 2), with their locations delineated using multiyear cropland data layers (CDLs) from the USDA National Agricultural Statistics Service (NASS). To ensure consistency with the DEM resolution, vector-type datasets such as the soil and land use maps were converted into grid-format datasets, with their spatial resolution set to 10 m. Detailed crop management schedules are available in Table S1 of the Supplementary Material.

Daily streamflow data spanning from 2010 to 2014 were acquired from the US Geological Survey (USGS) gauge station #01491500, located at the outlet of the TCW (Fig. 1a). Daily remotely sensed evapotranspiration (RS-ET) products were generated using the regional Atmosphere-Land Exchange Inverse (ALEXI) model [38], in conjunction with the associated flux spatial-temporal disaggregation scheme (DisALEXI) [39]. This multiscale modeling system is founded on the two-source energy balance model [40], which utilizes land surface temperature (LST) observations acquired via remote sensing to partition the available energy between latent and sensible heat fluxes emanating from the soil and canopy components of a scene. A data fusion algorithm integrates 30-m resolution bi-weekly ET retrievals from Landsat LST observations with 500-m resolution daily data from MODIS, resulting in fused datasets characterized by both high spatial and temporal resolutions [41]. In this study area, ALEXI/DisALEXI-driven RS-ET products were compared with in-situ eddy covariance flux tower measurements, demonstrating an average relative error of 10 % [35]. The temporal availability of the RS-ET products utilized in this study is from January 2010 to December 2014.

Daily LAI data with a spatial resolution of 500 m were derived from the MODIS Version 6 LAI/FPAR products (MCD15A3H). MCD15A3H represents a combined LAI product derived from two satellites (Terra and Aqua) at a temporal frequency of 4 days. For this study, MODIS LAI data products were procured from the National Aeronautics and Space Administration (NASA) and reprocessed to generate daily LAI data at USDA-ARS, Beltsville. The daily LAI values were acquired in two stages. Firstly, MODIS LAI quality control (QC) layers (FparLai_QC and FparExtra_QC) were utilized to eliminate LAI retrievals affected by partial clouds, cloud shadows, and dead detectors. Additionally, LAI retrievals from the physical radiative-transfer model (primary algorithm) and empirical model (secondary algorithm) were distinguished. Secondly, the 4-day MODIS LAI data obtained in the first stage were smoothed and interpolated to obtain daily LAI values using the Savitzky–Golay (SG) filter approach with a flexible fitting strategy [42]. Daily LAI values at a spatial resolution of 500 m were generated for the period from 2010 to 2014. In contrast to RS-ET, daily RS-LAI products were available with a spatial resolution of 500 m. Samples of RS-ET and RS-LAI are illustrated in Fig. S2 of the Supplementary Material.

The study watershed was partitioned into 19 sub-watersheds ranging in size from 0.09 to 32 km^2. During the generation of HRUs, the threshold area values for land use, soil, and slope were determined as >10 %, >15 %, and >15 %, respectively. The TCW comprised a total of 542 HRUs, encompassing 312 HRUs for cropland, 139 HRUs for forest, and 91 HRUs associated with other land use types. The sizes of the HRUs are from 10^{-6} to 7.21 km^2, with an average size of 0.41 km^2.

2.4. Model evaluations

The SWAT simulations were conducted at a daily temporal resolution from 2008 to 2014, considering the availability of RS-ET data from 2010 to 2014. While the simulation period of this study is relatively brief, it stands out from previous similar studies that predominantly utilized temporally coarse RS products (monthly or 8-day intervals) [10,14,15,27], as daily RS products were employed here. The difference of data temporal frequency would increase the value of this study. A multivariable calibration was performed using three observations: daily streamflow, watershed-level RS-ET, and RS-LAI. To test the degree of equifinality, this study counted the number of acceptable PARs as the three constraints (streamflow, RS-ET, and RS-LAI) were sequentially added. The initial two years (2008–2009) were allocated as spin-up periods, and the subsequent three years (2010–2012) were set for model calibration. Model

Table 2
Eight cultivation crop configurations in this study.

Type	2008	2009	2010	2011	2012	2013	2014	Proportion
1	WW/Soyb	Corn	WW/Soyb	Corn	WW/Soyb	Corn	WW/Soyb	14.5
2	Corn	WW/Soyb	Corn	WW/Soyb	Corn	WW/Soyb	Corn	21.9
3	WW/Soyb	Corn	Soyb	Corn	WW/Soyb	Corn	Soyb	7.7
4	Soyb	Corn	Soyb	Corn	Soyb	Corn	Soyb	11.3
5	Corn	Soyb	Corn	Soyb	Corn	Soyb	Corn	9.8
6	Corn	Corn	Corn	Corn	Corn	Corn	Corn	17.1
7	Corn	Soyb	Soyb	Corn	Soyb	Soyb	Corn	10.2
8	Soyb	Corn	Soyb	Soyb	Corn	Soyb	Soyb	7.5
Corn	59	58	49	61	56	51	59	56
Soyb	41	42	51	39	44	49	41	44

Note: WW/Soyb and Soyb indicate double-crop winter wheat, soybeans, and soybeans, respectively. The final column provides the relative area (%) corresponding to each crop rotation implemented in the croplands. The last two rows depict the relative areas (%) allocated to corn and soybean fields resulting from various concurrent rotations. The spatial distribution of the eight representative cropland rotations is illustrated in Fig. S1 of the Supplementary Material.

validation was then executed over the remaining two years (2013–2014).

At the watershed level, model calibration was conducted utilizing streamflow data, alongside watershed-level RS–ET and RS–LAI data to identify PARs-1 (satisfactory performances for streamflow and RS-ET) and PARs-2 (satisfactory performances for streamflow, RS-ET, and RS-LAI) (Section 2.4.1). Then, a spatial evaluation was conducted at the sub-watershed (section 2.4.2) using simulations from PARs-2.

2.4.1. Model calibration at the watershed level

The SWAT model has been extensively utilized in the study area, as shown in previous studies [5,11]. These have reported sensitive parameters with their ranges and optimal values that yield satisfactory performance metrics, as outlined in Moriasi, 2007 [43]. Regarding previous studies, we identified 13 hydrologic parameters that were demonstrated to be sensitive within this study. Furthermore, seven vegetation parameters were selected to calibrate the LAI values of corn, soybean, and forest following previous studies [44]. Calibration of tree vegetation types was considered, as they accounted for over 90 % of the watershed's composition.

Adjustments were made to the parameters associated with corn and soybean, as the distribution and rotation of these two crops were accurately represented by the land use map utilized in this study. Detailed cultivation practices, such as fertilizer application timing and quantity, planting, and harvesting schedules, for these two crops were established in collaboration with local experts [37]. Therefore, our simulations accurately depicted the growth dynamics of corn and soybean. Regarding the crop growth pattern, seasonal dynamics of LAI simulations were expected: high LAI during the summer season (May to October) and low LAI during the winter season (November to April). These LAI dynamics would be confirmed by the simulated LAI data calibrated against RS-LAI. the calibration

Table 3
The list of calibrated parameters with their descriptions, allowable ranges, and sensitivity ranking.

Parameter	Description (units)	Range	Sensitivity ranking	
			RS-ET	RS-LAI
CN[!]	SCS runoff curve number	−20 – 20 %	1	10
GW_DELAY[!]	Groundwater delay (days)	0–500	26	34
ALPHA_BF[!]	Baseflow alpha factor ($days^{-1}$)	0–1	32	30
GWQMN[!]	Threshold depth of water in the shallow aquifer required for return flow to occur (mm H_2O)	0–5000	33	31
GW_REVAP[!]	Groundwater "revap" coefficient	0.02–0.2	24	23
REVAPMN[!]	Threshold depth of water in the shallow aquifer for "revap" to occur (mm H_2O)	0–1000	29	27
SOL_AWC[!]	Available water capacity of the soil layer (mm H_2O ·mm $soil^{-1}$)	−50 – 50 %	2	26
CH_K2*	Effective hydraulic conductivity in the main channel alluvium	0–500	31	22
CH_N2*	Manning's "n" value for the tributary channels	0.01–0.3	28	28
SURLAG[$]	Surface runoff lag coefficient	0.5–24	30	29
ESCO[!]	Soil evaporation compensation factor	0–1	13	25
EPCO[!]	Plant uptake compensation factor	0–1	3	20
CANMX[!]	Maximum canopy storage (mm H_2O)	0–100	4	18
BIO_E[!] (corn)	Radiation use efficiency in ambient CO_2 ((kg/ha)/(MJ/m^2))	10–90	27	19
BIO_E[!] (soybean)			21	33
BIO_E[!] (forest)			25	13
BLAI[!] (corn)	Maximum potential leaf area index (m^2m^{-2})	0.5–10	9	3
BLAI[!] (soybean)			12	4
BLAI[!] (forest)			20	1
FRGRW1[!] (corn)	Fraction of the plant growing season of total potential heat units corresponding to the first point on the	0–0.5	22	8
FRGRW1[!] (soybean)	leaf area development curve		23	9
FRGRW1[!] (forest)			34	7
FRGRW2[!] (corn)	Fraction of the plant growing season of total potential heat units corresponding to the second point on the	0.5–1	15	17
FRGRW2[!] (soybean)	leaf area development curve		14	15
FRGRW2[!] (forest)			16	16
LAIMX1[!] (corn)	Fraction of the maximum leaf area index corresponding to the first point on the leaf area development	0–0.5	18	12
LAIMX1[!] (soybean)	curve		17	14
LAIMX1[!] (forest)			19	11
LAIMX2[!] (corn)	Fraction of the maximum leaf area index corresponding to the second point	0.5–1	11	32
LAIMX2[!] (soybean)			8	21
LAIMX2[!] (forest)			7	24
DLAI[!] (corn)	Leaf to biomass fraction	0.15–1.00	5	6
DLAI[!] (soybean)			10	5
DLAI[!] (forest)			6	2

Note: !, *, and $ denote parameters with values varying across HRUs, sub-watersheds, and watersheds, respectively. Changes in parameters were performed by relative adjustments for CN2 and SOL_AWC, while the remaining parameters underwent replacement. The gray box highlights the top ten sensitive parameters. RS-ET and RS-LAI denote remotely sensed evapotranspiration and leaf area index, respectively. Calibrated parameter values can be found in Table S3 of the Supplementary Material.

process did not include double-cropped soybean, as the information described above primarily related to summer crops. The calibrated parameters and their permissible ranges are listed in Table 3.

For model calibration, a set of 20,000 PARs was generated using Latin hypercube sampling (LHS). The LHS method partitions the parameter sampling space into multiple non-overlapping subspaces with equal probabilities [18]. Subsequently, within each subspace, individual parameter values are randomly selected to compose a PAR, ensuring that each subspace contributes only one value to each PAR [18]. LHS is recognized for its efficacy in converging towards the optimal PAR relative to random sampling methods [14]. The parameter values were altered through manual calibration, employing relative adjustments for only two parameters (CN2 and SOL_AWC) and replacement for the remaining parameters. Following parameter adjustments and model simulations, the daily model outputs (streamflow, ET, and LAI) were simultaneously compared with corresponding observations. For this study, the Kling-Gupta Efficiency (KGE) was chosen as the model performance metric, given its widespread adoption in SWAT modeling studies incorporating RS-ET and RS-LAI. Additionally, to evaluate equifinality, consistent performance measures across all observations were employed. KGE is computed as follows (Eq. (4))

$$\mathrm{KGE} = 1 - \sqrt{(r-1)^2 + (\sigma_s/\sigma_o - 1)^2 + (\mu_s/\mu_o - 1)^2} \tag{4}$$

where, r indicates the Pearson product-moment correlation coefficient, σ_s/σ_o and μ_s/μ_o indicate the variability ratio and bias between simulations and observations, respectively, σ and μ are the standard deviation and mean of the variables, respectively. The subscripts s and o indicate simulations and observations, respectively. KGE values span from negative infinity to 1, with values approaching 1 denoting higher model performance.

KGE computation was made by the "hydroeval" package within the Python 3.8.12 program [45]. This study set acceptable daily model performance measures as follows: streamflow (KGE >0.55), ET, and LAI (KGE >0.5), with relaxed criteria relative to streamflow based on previous studies [46,47].

Discerning parameters significantly impacting ET and LAI simulations could offer valuable insights into the efficacy of incorporating two additional remotely sensed constraints. Initially, parameter sensitivity analyses were conducted separately for RS-ET and RS-LAI. A global sensitivity method entailed fitting a linear relationship between the objective function and parameter values [48]. The KGE values for watershed-level ET and LAI during the calibration period served as the objective function for the global sensitivity analyses to identify sensitive parameters for RS-ET and RS-LAI, respectively. Subsequently, coefficients of variation (CV) were computed for the top ten sensitive parameters for RS-ET and RS-LAI, respectively. CV, defined as the standard deviation divided by the mean value, has been commonly employed to quantify parameters' impacts on simulation outcomes [18,49]. Additionally, overall model uncertainty was evaluated using the P-factor and R-factor. The P-factor denotes the proportion of observations within the 95 % prediction uncertainty (95 PPU) computed at the 2.5 and 97.5 percentiles of the cumulative distribution of all simulations. The R-factor means the average width of the 95 PPU bands relative to the standard deviation of the observations. The R-factor ranges from 0 to infinity, while the P-factor ranges from 0 to 100 %.

2.4.2. Model calibration at the sub-watershed level

The modeled ET and LAI were assessed against RS-ET and RS-LAI products at the sub-watershed level. The RS-ET and RS-LAI datasets were delineated by the sub-watershed boundaries derived from the ArcSWAT process. The TCW encompassed 19 sub-watersheds. Excluding one sub-watershed smaller than the LAI pixel size (0.25 km^2), 18 sub-watersheds were utilized for sub-watershed-level spatial assessments. These evaluations were executed utilizing simulations from PARs-1 and PARs-2. For each individual sub-watershed, KGE values were computed for ET and LAI. PARs with median KGE values exceeding 0.5 for both ET and LAI

Table 4
Model performance measures for daily streamflow, RS-ET, and RS-LAI.

PAR	Streamflow		RS-ET		RS-LAI	
	Calibration	Validation	Calibration	Validation	Calibration	Validation
	KGE	KGE	KGE	KGE	KGE	KGE
1	0.71	0.60	0.53	0.57	0.45	0.55
2	0.73	0.56	0.51	0.58	0.10	0.11
3	0.73	0.56	0.54	0.58	0.55	0.69
4	0.66	0.57	0.56	0.57	0.58	0.67
5	0.77	0.60	0.52	0.59	0.50	0.57
6	0.66	0.62	0.55	0.56	0.41	0.43
7	0.63	0.57	0.52	0.57	0.27	0.29
8	0.68	0.59	0.50	0.56	0.48	0.55
9	0.59	0.59	0.53	0.58	0.51	0.57
10	0.60	0.58	0.60	0.61	0.22	0.34
11	0.72	0.59	0.56	0.57	0.48	0.57
12	0.60	0.58	0.53	0.58	0.57	0.70
13	0.68	0.56	0.51	0.57	0.62	0.77
14	0.63	0.58	0.52	0.58	0.56	0.69

Note: PAR indicates a parameter set. The six shaded rows (#3, 4, 9, 12, 13, and 14) are PARs-2.

were deemed to exhibit satisfactory performance concerning the spatial distribution of ET and LAI at the sub-watershed level. Conversely, PARs failing to meet these criteria were considered inadequate in capturing the spatial distribution of ET and LAI at the sub-watershed level, notwithstanding acceptable performance at the watershed level. These evaluation outcomes were subsequently utilized to further assess the equifinality.

3. Results and discussion

3.1. Watershed-level simulations and parameter uncertainty

The calibration outcomes at the watershed level reveal the existence of 14 PARs-1 and 6 PARs-2 (Table 4). For PARs-1, the KGE values ranged from 0.59 to 0.77 (0.56–0.62) for streamflow and from 0.50 to 0.60 (0.56–0.61) for RS-ET during the calibration (validation) period (Table 4). Notably, the six PARs (PARs-2) were identified to concurrently meet the model performance thresholds

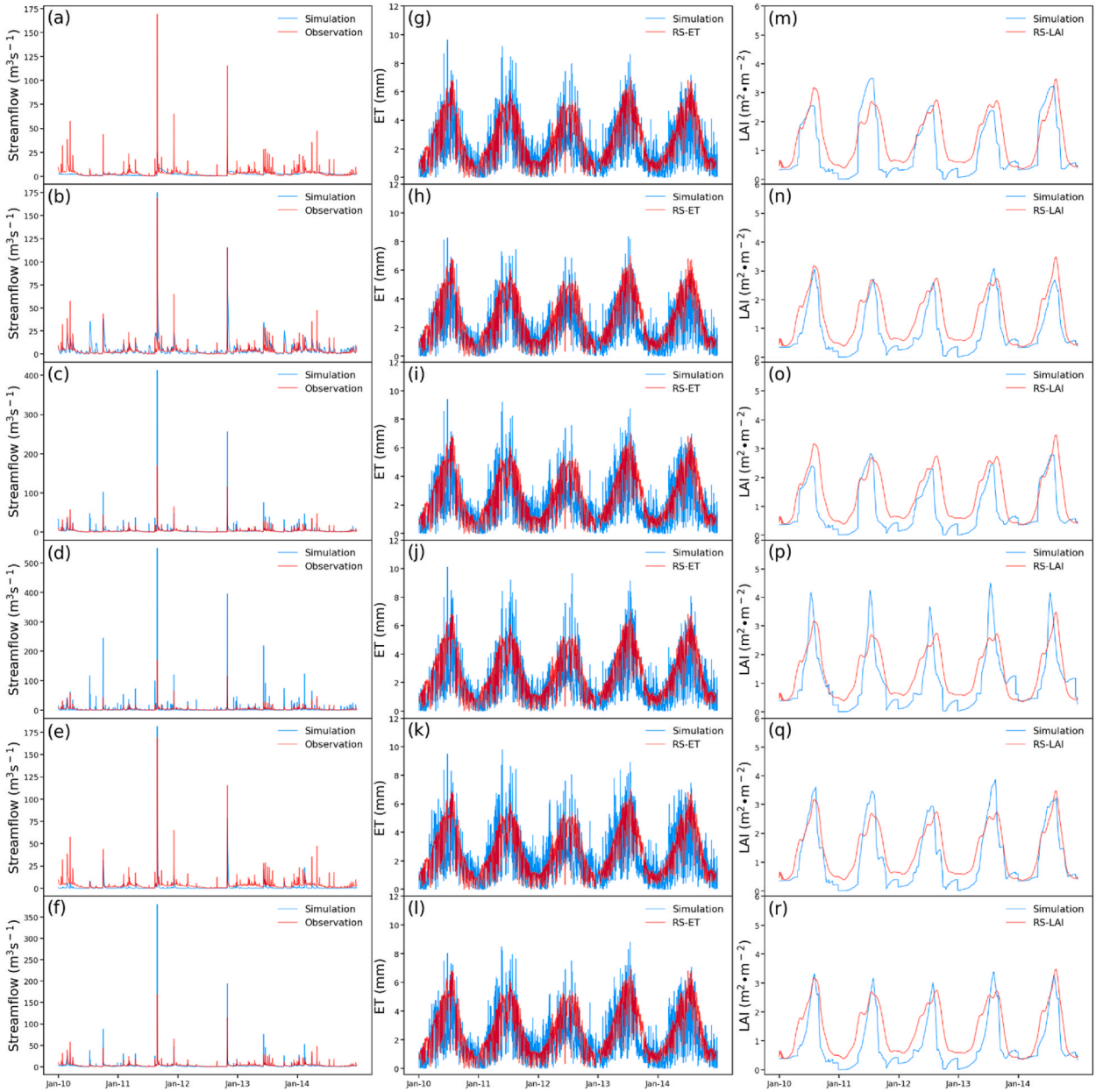

Fig. 2. Daily simulated and observed streamflow, watershed-level RS-ET, and RS-LAI from 2010 to 2014: PAR #3 (a, g, and m), #4 (b, h, and n), #9 (c, i, and o), #12 (d, j, and p) #13 (e, k, and q) #14 (f, l, and r). The extended illustration is included in Fig. S3 of the Supplementary Material.

for streamflow, RS-ET, and RS-LAI (Table 4). Specifically, the model performance measures for PARs-2 ranged from 0.59 to 0.73 (0.56–0.59) for streamflow, 0.51 to 0.56 (0.57–0.58) for RS-ET, and 0.51 to 0.62 (0.57–0.77) for RS-LAI during the calibration (validation) period.

The optimal parameters used for the leaf area development curve noticeably differed between PARs-1 and PARs-2. Overall, the PARs-2 had greater values for the parameters (i.e., LAIMX2 and FRGRW2) that support plant growth during longer growth periods and achieve greater LAI than PARs-1. Greater maximum potential leaf area index (BLAI) values were found in PARs-2 compared to PARs-1, which also contributed to greater LAI. These differences may result in better depictions of actual LAI by PARs-2.

The incorporation of RS-LAI resulted in a notable reduction in equifinality, decreasing from 14 to 6. Despite the inclusion of RS-LAI, a 50 % reduction in equifinality was found, primarily attributed to the consideration of LAI in both ET calculation and RS-ET retrieval processes. In this study, the Penman-Monteith method employed for ET calculation relied on canopy resistance as a key parameter, which was determined based on LAI within the SWAT [33]. Moreover, RS-LAI data served as inputs for RS-ET retrievals [35]. Consequently, calibrated parameter sets demonstrating agreement with RS-ET could effectively capture LAI dynamics as well. This aligns with findings from a prior study by Chen, 2017 [50], which also highlighted a strong correlation between ET and LAI derived from SWAT simulations.

Observed streamflow, RS-ET, and RS-LAI were compared with simulation results from PARs-2 (Fig. 2). While the simulated streamflow failed to depict observed peak flows throughout the simulation period (Fig. 2a–f), this discrepancy might stem from the SWAT model's limitation capturing precipitation intensity and duration in its surface runoff calculation, leading to an underestimation of peak streamflow [51]. Conversely, ET and LAI exhibited seasonal trends, peaking during the summer (May to October) and declining during the winter (November to April) (Fig. 2g-r). This seasonal variation aligns with a previous study [52] and local tower measurements [35], reflecting the influence of warm temperatures and plant growth on peak ET and LAI values during summer. The simulated LAI calibrated by RS-LAI verified the seasonal patterns in LAI for this study site.

Relative to streamflow and RS-LAI, low KGE values were found in ET simulations (Table 4). This discrepancy might be attributed to the omission of irrigation practices in our simulations due to insufficient associated information. In contrast, thermal ET remote sensing directly identifies irrigation effects on ET [53], and a previous study indicated an improved ET simulation accuracy with inclusion of irrigation practices [50]. Additionally, depressional wetlands prevalent in forested areas likely contributed to water loss via ET at rates higher than those simulated by the SWAT model, possibly leading to the observed discrepancies in ET (Fig. 2g–i) [54]. Furthermore, the SWAT model's structural limitations in simulating evaporation on wet canopies might impede the accurate

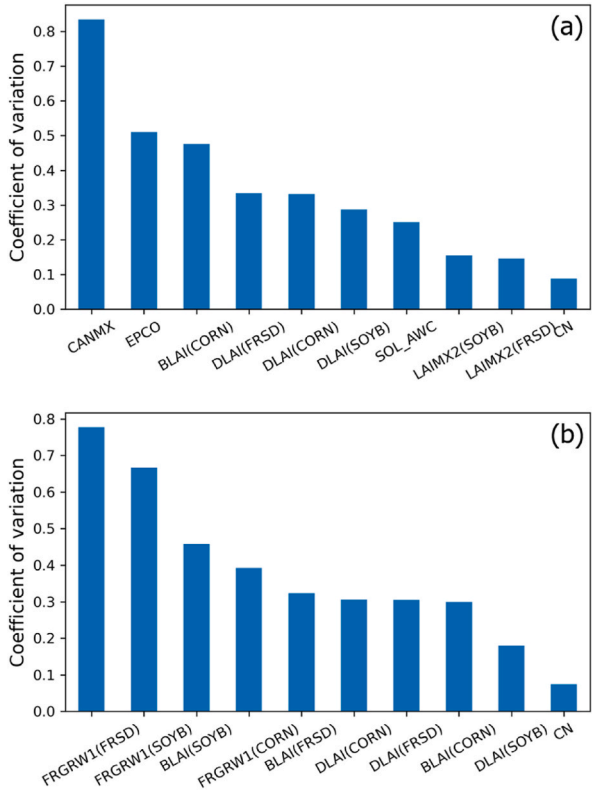

Fig. 3. The coefficient of variation (CV) values for the top ten sensitive parameters related to RS-ET (a) and RS-LAI (b). Note: (a) denotes the CV for PARs-1, comprising 14 parameter sets acceptable for streamflow and RS-ET. (b) illustrates the CV for PARs-2, encompassing 6 parameter sets acceptable for streamflow, RS-ET, and RS-LAI.

simulation of ET [55].

Simulated LAI values predominantly fell below observations during winter (Fig. 2m-r), possibly due to the absence of winter cover crops implemented in the region. Winter cover crops tended to enhance the vegetation index during the winter seasons [56]. The exclusion of winter cover crops from simulations might lead to underestimated LAI during winter. Adjusting the range of LAI parameters based on available in-situ observations could improve the accuracy of future LAI simulations, suggesting careful consideration in subsequent studies.

3.2. Parameter and model uncertainty

The CV values was calculated for the top ten sensitivity parameters regarding RS-ET and RS-LAI using PARs-1 and PARs-2, respectively (Fig. 3). The sensitivity ranking is shown in Table 3. Among the 14 PARs acceptable for streamflow and RS-ET (i.e., PARs-1), the parameter governing maximum canopy storage (CANMX) exhibited the highest CV value for RS-ET (Fig. 3a). Conversely, for the 6 PARs acceptable for streamflow, RS-ET, and RS-LAI (i.e., PARs-2), the parameter controlling forest leaf area development (FRGRW1) demonstrated the highest CV value (Fig. 3b). The CANMX and FRGRW1 values displayed broader distributions relative to the parameters of PARs-1 and PARs-2, respectively.

The calibration outcomes, constrained by streamflow and RS-ET, showed the highest sensitivity to maximum canopy storage. Given that canopy evaporation is the initial consideration in the calculation of actual ET within the SWAT model [33], CANMX likely exhibited the most noticeable variability (Fig. 3a). Conversely, when SWAT was calibrated against streamflow, RS-ET, and RS-LAI, the parameter associated with leaf area development was shown as the most influential among PARs-2 parameters. Considering the prevalence of forest cover, accounting for 32.8 % of the study area, compared to approximately 27 % covered by corn and soybean, the forest-related parameter yielded the highest CV value (Fig. 3b).

The overall model uncertainty was represented as P-factor and R-factor (Table 5). Regarding the P-factor values, most observed streamflow was within the 95 PPU while observed RS-ET and RS-LAI were far from the band. Based on the R-factor values, the width of the uncertainty band was narrowest for ET, followed by LAI and streamflow.

3.3. The spatial distribution of ET and LAI at the sub-watershed level

The KGE values of daily ET and LAI were computed for each sub-watershed (Figs. 4 and 5). The range of the median KGE values for ET was from 0.51 to 0.55 and from 0.57 to 0.58 during the calibration and validation periods, respectively (Fig. 4ab). LAI predictions tended to have lower KGE values (0.46–0.57 for the calibration period and 0.54–0.57 for the validation period) compared to ET predictions (Fig. 4cd). While all PARs-2 exhibited satisfactory performance measures for the sub-watershed-level ET criteria, only three PARs-2 (#4, #13, and #14) surpassed the sub-watershed-level LAI criteria (KGE >0.5). Overall, discrepancies in KGE values across sub-watersheds were observed likey due to diverse land cover types at the sub-watershed level impacting ET and LAI.

The PAR#12 exhibited increased KGE values for LAI (0.57 and 0.70 for the calibration and validation periods, respectively) at the watershed level. However, its KGE values at the sub-watershed level were lower with 0.46 and 0.54 for the calibration and validation periods, respectively (as depicted in Figs. 2 and 4). Like PAR#12, both PAR#3 and #9 cases represented acceptable KGE values at the watershed level but showed unacceptable for the sub-watershed-level criteria for LAI. The sub-watershed outcomes indicated a reduction in the number of acceptable PARs from six (PARs-2) to three. This results suggested that the sub-watershed-level evaluation aided in identifying PARs that adequately represented internal processes at a finer spatial scale. This result supported the notion that spatialized evaluation using remotely sensed data can further constrain the number of acceptable PARs, consequently mitigating predictive uncertainty (e.g., equifinality).

Among PARs-1, those unacceptable for LAI performance tended to have low values of maximum potential leaf area index (BLAI). Among the PARs unacceptable for LAI performance, the PAR (PAR #3) with the greater BLAI values for three vegetations (i.e., corn, soybean, and forest) represented the best performance. Interestingly, among the PARs acceptable for LAI performance, the best performance was observed in the PAR (PAR #4) with greater BLAI values. Overall, the simulated LAI was lower than observed likely due to low BLAI values, leading to decreased LAI performance.

The KGE values of three PARs-2 acceptable for sub-watershed-level ET and LAI were mapped for each sub-watershed (Fig. 5). The range of KGE values for sub-watershed-level ET was between 0.45 and 0.60 (Fig. 5a–c), and the overall KGE values were decent. However, the range of KGE values for sub-watershed-level LAI was between 0.35 and 0.80 (Fig. 5d–e). Overall, the sub-watersheds with the large KGE values for LAI were dominated by a greater proportion of cropland types #1 and #2 types. These two cropland

Table 5
P-factor and R-factor for streamflow, ET, and LAI.

Variable	Period	P-factor	R-factor
Streamflow	Calibration	0.99	1.18
	Validation	0.97	2.01
ET	Calibration	0.31	0.82
	Validation	0.31	0.75
LAI	Calibration	0.24	1.04
	Validation	0.37	1.05

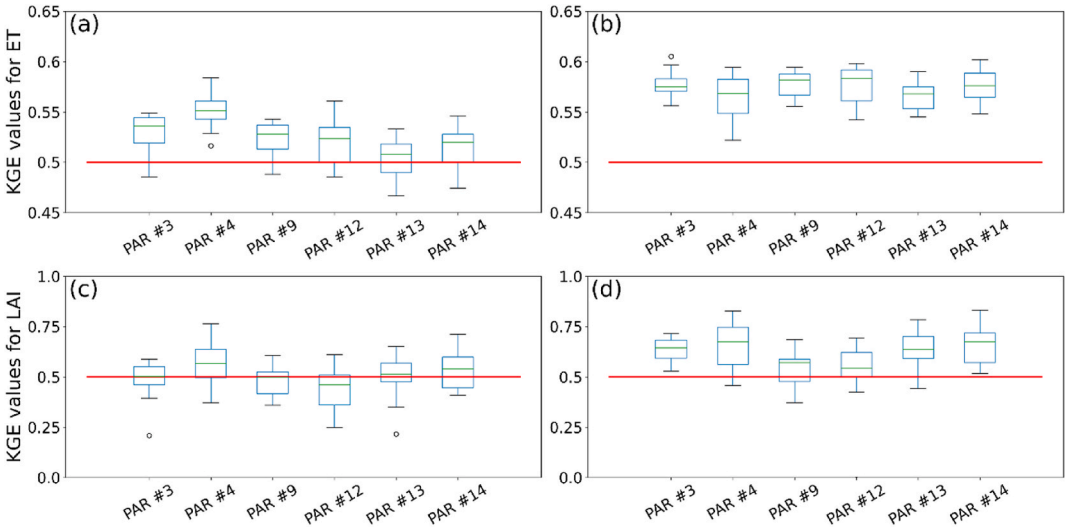

Fig. 4. Median KGE values across sub-watersheds: (a) ET for calibration, (b) ET for validation, (c) LAI for calibration (d) LAI for validation. A KGE threshold of 0.5 is denoted by the horizontal red line. Detailed KGE values for individual sub-watersheds are found in Tables S4 and S5 of the Supplementary Material for ET and LAI, respectively.

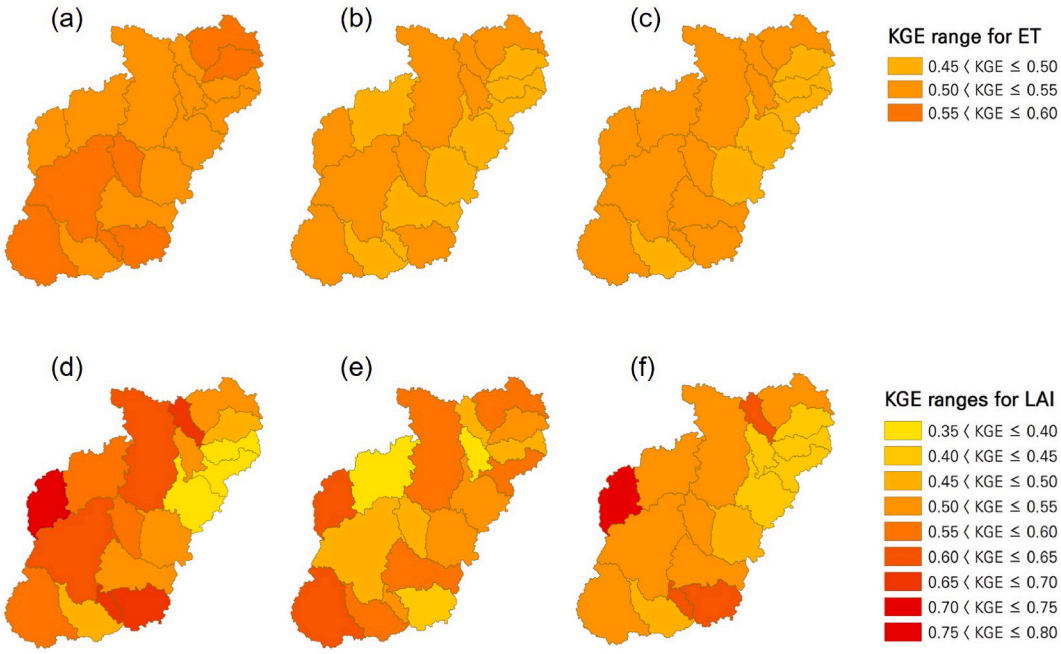

Fig. 5. The sub-watershed level KGE values for the PAR#4, PAR#13, and PAR#14: ET (a, b, and c) and LAI (d, e, and f). Note: The figure was created by ArcMap 10.7 program (https://www.esri.com/en-us/arcgis/products/arcgis-desktop/resources).

types included winter wheat during every winter season, which might reduce the gap between simulations and observations during winter seasons. In contrast, other cropland types have no or few crops during winter seasons. The simulated LAI tended to be lower than observed values, especially during the winter seasons (Fig. 3). Therefore, crops planted during winter seasons could minimize the differences between simulated and observed LAI.

All PARs-2 successfully met the criterion for ET at the sub-watershed level, while half of them satisfied the criteria for LAI. This discrepancy could be attributed to the differing spatial resolutions of RS-ET and RS-LAI. RS-ET, with its finer 30 m resolution, might better capture sub-watershed-level ET dynamics, whereas RS-LAI, with a coarser 500 m resolution, might not adequately resolve variations in LAI at the sub-watershed level compared to the watershed level.

While spatialized parameterization demands significant computational resources and prolonged simulation times, it offers valuable

insights into large watershed dynamics [17,46]. However, our study site was relatively small spatial extent (220 km^2) compared to previous studies (>1670 km^2). This suggested that a lumped parameterization is sufficient for our aim of leveraging multiple remotely sensed datasets to mitigate predictive uncertainty and assess the spatial distribution accuracy of ET and LAI.

4. Implications and limitations

This study incorporated two remotely sensed products to enhance model prediction accuracy. Our study offered valuable insights into watershed modelingg with multiple additional remotely sensed products, despite their advantages having been reported in previous studies [57,58]. Our study demonstrated the advantages of using these additional remotely sensed ET and LAI products to constrain SWAT parameters, with an emphasis on reducing equifinality and spatial calibration. Previous studies have investigated SWAT improvements using RS-ET or RS-LAI by replacing SWAT simulations with remotely sensed products or using single remotely sensed products [10,59,60]. Several studies adopted both types of remotely sensed data [27,57,61]. However, our study differed from these previous studies in the type of remotely sensed products and hydrologic models used, the major roles of the remotely sensed products, or in the application purposes (Table 6). Although the two studies [27,29] showed similar approaches of this study, the spatial areas differed and our study demonstrated the benefits of two remotely sensed data at a finer temporal scale (i.e., daily) compared to previous studies (i.e., monthly). All nine studies, including this study, have focused on the usefulness of using remotely sensed products to emhance hydrologic modeling (Table 6). Future studies would gain new insights from the methods and results from each individual study. Furthermore, the study site is located on the CBW, a unique watershed in the U.S. with extensive scientific studies and investment. Therefore, this work is not only a scientific practice but can also be applied in critical regions of a fully developed country. Our study also showed the reduction of SWAT uncertainty with daily remotely sensed products. Daily remotely sensed products are not common, but the continuous advancement of satellite monitoring techniques could offer high-temporal resolution remotely sensed products, contirbuting to enhancing SWAT simulations.

The conventional hydrologic practices select a sole PAR demonstrating optimal model performance during calibration and validation. This selected PAR is subsequently employed to accomplish objectives [28]. However, this approach definitely includes uncertainty. In contrast, several studies presented a spectrum of predicted outcomes derived from all PARs exhibiting acceptable performance metrics, rather than relying on a single prediction output [63–65]. The use of remotely sensed products provides an opportunity to reduce parameter uncertainty, as they are freely available [11]. Thus, remotely sensed products would supplment the weakness of the conventional hydrologic practices.

The use of low-resolution RS-LAI products in this study could not be free from data imperfections and equifinality issues, but RS-LAI with a 500-m resolution can effectively constrain the SWAT model [21]. It should be noted that the additional use of RS-LAI could

Table 6
Comparisons between this study and previous studies.

Literature	Remotely sensed products	Model	Major roles of RS products	Application purposes
Parr, 2015 [57]	RS-ET (AVHRR and ISLSCP-II) RS-LAI (MODIS)	VIC	LAI as inputs; ET used to bias correct VIC simulations	Improving hydrologic simulation in large river basin
Ha, 2018 [29]	RS-ET (Ensemble data) RS-LAI (MOD-15)	SWAT	Uncertainty analysis	Improving model accuracy in Vietnam
Albergel, 2017 [61]	RS-Soil moisture (ESA CCI SM) RS-LAI (GEOV1 LAI)	A global land surface model (LDAS-Monde)	Sequential assimilation of soil moisture and LAI	Improving continental scale simulations of river discharge, spatial ET and gross primary production
Ines, 2013 [62]	RS-Soil moisture (AMSR-E) RS-LAI (MODIS)	DSSAT-CSM	Sequential assimilation of soil moisture and LAI	Improving crop yield prediction at the county scale.
Rajib, 2018 [59]	RS-ET (MODIS)	SWAT	Injecting RS-PET into SWAT	Improving simulations of soil moisture, AET and streamflow in small to medium-sized watersheds
Rajib, 2020 [21]	RS-LAI (MODIS)	SWAT	Replacing SWAT simulated LAI with RS observations	Improving simulations of soil moisture, streamflow and nitrate loads in a medium-sized watershed
Ma, 2019 [10]	RS-LAI (MODIS)	SWAT	Replacing SWAT simulated LAI with RS observations	Improving simulations of streamflow and sediments in a small watershed
Rane, 2023 [27]	RS-ET (MODIS) RS-LAI (MODIS)	SWAT	Uncertainty analysis	Improving model predictions with additional data in India
This study	RS-ET (ALEXI) RS-LAI (MODIS)	SWAT	Using LAI and ET for reducing parameter equifinality reduction and spatial calibration	Improving simulations of spatial LAI and ET in a small watershed

Note: Advanced Very High Resolution Spectroradiometer (AVHRR); International Satellite Land-Surface Climatology Project, Initiative II (ISLSCP-II); Variable Infiltration Capacity (VIC); European Space Agency (ESA); Climate Change Initiative (CCI); Advanced Microwave Scanning Radiometer (AMSR-E); Moderate Resolution Imaging Spectroradiometer (MODIS); DSSAT-CSM: Decision Support System for Agro-technology Transfer – Cropping System Model; SWAT: Soil and Water Assessment Tool; Atmosphere-Land Exchange Inverse (ALEXI).

better capture equifinality compared to not using it. Similar to previous similar studies [21,27], the validation of RS-LAI was not tested in this study site, although RS-LAI agreed with observed season trends. Most similar previous studies that used either RS-ET or RS-LAI for SWAT calibrations showed improved model performances when using remotely sensed data although the accuracy of remotely sensed products was not confirmed with ground truth [10,21,27,59,66]. Relative to the number of the SWAT parameters, available observational data are extremely limited [1]. The addition of remotely sensed products to SWAT calibrations is meaningful in hydrologic modeling. However, the impacts of non-validation data on the SWAT calibration results remain unknown. Therefore, the impacts of remotely sensed products (validated vs. non-validated and high vs. low spatial resolutions) on SWAT modeling would also be needed in future studies.

Model performance measures have been explored in previous studies [43]. However, the measures for ET and LAI might vary depending on temporal scales. Daily simulations of ET and LAI were frequently quantified using single measurement (e.g., KGE) [17,21]. For monthly simulations, multiple measures including KGE are commonly used [15,16,18,67,68]. Depending on the temporal resoltions of the simulated results, less or strict criteria were suggested for the streamflow predictions. In contrast, the performance measures for ET and LAI have been rarely investigated when using remotely sensed products for watershed modeling. Futhre studies would be neede to provide guidelines for selecting suitable performance measures for remotely sensed products.

Nevertheless, this study presented several limitations that deliver consideration in future studies. While remotely sensed products offer the advantage of evaluating hydrological models at a more detailed spatial resolution compared to data collected at the watershed outlet, they inherently included uncertainties greater than those in conventional observations [69]. Hence, it's imperative to account for the inherent uncertainty associated with remotely sensed products when integrating them into watershed modeling frameworks. Moreover, the ET and LAI simulations are substantially influenced by climatic data. In this study, three sets of climatic input data—namely humidity, solar radiation, and wind speed—were generated using SWAT's built-in weather generator, following previous studies [70]. However, the utilization of grid-format continuous climate datasets, which are increasingly available, holds potentials for enhancing model predictions of ET and LAI [71,72].

5. Conclusion

This study incorporated remotely sensed evapotranspiration (RS-ET) and leaf area index (RS-LAI) as additional constraints to enhance SWAT simulations. Initially, the SWAT model calibration was conducted using observed streamflow and RS-ET, and then the calibrated model was refined by integrating RS-LAI to assess the impact of RS-LAI on acceptable parameter sets (PARs). Subsequently, the efficacy of spatial calibration using remotely sensed products in capturing the spatial distribution of ET and LAI at the sub-watershed level was explored. The findings revealed that the calibration against both RS-ET and RS-LAI and spatial calibration contributed to a reduction in the number of acceptable PARs, thereby mitigating parameter uncertainty.

This study highlighted the impact of integrating RS-ET and RS-LAI on predictive uncertainty. Furthermore, the utilization of remotely sensed products allowed spatial assessments at finer resolutions, resulting in diminished predictive uncertainty and enhanced characterization of intra-watershed dynamics. These results demonstrated the necessity of integrating remotely sensed data as additional constraints to mitigate uncertainty in watershed models, enhancing their applicability in watershed modeling.

Disclaimer

The U.S. Department of Agriculture is an equal opportunity provider and employer. Any use of trade, firm, or product names is for descriptive purposes only and does not imply endorsement by the U.S. Government.

Data availability

According to the request, the dataset used in this study are available from the corresponding author.

CRediT authorship contribution statement

Sangchul Lee: Writing – review & editing, Writing – original draft, Validation, Supervision, Software, Investigation, Data curation, Conceptualization. **Dongho Kim:** Visualization. **Gregory W. McCarty:** Resources. **Martha Anderson:** Resources, Data curation. **Feng Gao:** Resources, Data curation. **Fangni Lei:** Resources, Data curation, Resources. **Xuesong Zhang:** Resources, Data curation, Conceptualization. **Haw Yen:** Conceptualization. **Junyu Qi:** Conceptualization. **Wade Crow:** Resources, Data curation. **In-Young Yeo:** Resources. **Liang Sun:** Resources, Data curation.

Declaration of competing interest

The authors declare that they have no known competing financial interests or personal relationships that could have appeared to influence the work reported in this paper.

Acknowledgments

This work was supported by a Korea University Grant, and the United States Department of Agriculture (USDA) Natural Resources

Conservation Service, in association with the Wetland Component of the National Conservation Effects Assessment Project. This research was a contribution from the Long-Term Agroecosystem Research (LTAR) network. LTAR is supported by the USDA.

Appendix A. Supplementary data

Supplementary data to this article can be found online at https://doi.org/10.1016/j.heliyon.2024.e30923.

References

[1] M. Leong Tan, P.W. Gassman, X. Yang, J. Haywood, A review of SWAT applications, performance and future needs for simulation of hydro-climatic extremes, Adv. Water Resour. 143 (2020) 103662, https://doi.org/10.1016/j.advwatres.2020.103662.
[2] J. Seibert, J.J. McDonnell, On the dialog between experimentalist and modeler in catchment hydrology: use of soft data for multicriteria model calibration, Water Resour. Res. 38 (2002) 1241, https://doi.org/10.1029/2001wr000978.
[3] J.G. Arnold, M.A. Youssef, H. Yen, M.J. White, A.Y. Sheshukov, A.M. Sadeghi, D.N. Moriasi, J.L. Steiner, D.M. Amatya, R.W. Skaggs, E.B. Haney, J. Jeong, M. Arabi, P.H. Gowda, Hydrological processes and model representation: impact of soft data on calibration, Trans. ASABE (Am. Soc. Agric. Biol. Eng.) 58 (2015) 1637–1660, https://doi.org/10.13031/trans.58.10726.
[4] H. Yen, M.J. White, J.C. Ascough, D.R. Smith, J.G. Arnold, Augmenting watershed model calibration with incorporation of Ancillary data sources and qualitative soft data sources, J. Am. Water Resour. Assoc. 52 (2016) 788–798, https://doi.org/10.1111/1752-1688.12428.
[5] S. Lee, I.-Y. Yeo, M.W. Lang, G.W. McCarty, A.M. Sadeghi, A. Sharifi, H. Jin, Y. Liu, Improving the catchment scale wetland modeling using remotely sensed data, Environ. Model. Software 122 (2019) 104069, https://doi.org/10.1016/j.envsoft.2017.11.001.
[6] H. Yen, R.T. Bailey, M. Arabi, M. Ahmadi, M.J. White, J.G. Arnold, The role of interior watershed processes in improving parameter estimation and performance of watershed models, J. Environ. Qual. 43 (2014) 1601–1613, https://doi.org/10.2134/jeq2013.03.0110.
[7] K.B. Vaché, J.J. McDonnell, A process-based rejectionist framework for evaluating catchment runoff model structure, Water Resour. Res. 42 (2006), https://doi.org/10.1029/2005WR004247.
[8] S. Julich, L. Breuer, H.G. Frede, Integrating heterogeneous landscape characteristics into watershed scale modelling, Adv. Geosci. 31 (2012) 31–38, https://doi.org/10.5194/adgeo-31-31-2012.
[9] P.W. Gassman, A.M. Sadeghi, R. Srinivasan, Applications of the SWAT model special section: overview and insights, J. Environ. Qual. 43 (2014) 1–8, https://doi.org/10.2134/jeq2013.11.0466.
[10] T. Ma, Z. Duan, R. Li, X. Song, Enhancing SWAT with remotely sensed LAI for improved modelling of ecohydrological process in subtropics, J. Hydrol. (Amst.) 570 (2019) 802–815, https://doi.org/10.1016/J.JHYDROL.2019.01.024.
[11] I.-Y. Yeo, S. Lee, M.W. Lang, O. Yetemen, G.W. McCarty, A.M. Sadeghi, G. Evenson, Mapping landscape-level hydrological connectivity of headwater wetlands to downstream waters: a catchment modeling approach - Part 2, Sci. Total Environ. 653 (2019) 1557–1570, https://doi.org/10.1016/j.scitotenv.2018.11.237.
[12] B. Uniyal, J. Dietrich, C. Vasilakos, O. Tzoraki, Evaluation of SWAT simulated soil moisture at catchment scale by field measurements and Landsat derived indices, Agric. Water Manag. 193 (2017) 55–70, https://doi.org/10.1016/j.agwat.2017.08.002.
[13] D. Jiang, K. Wang, The role of satellite-based remote sensing in improving simulated streamflow: a review, Water (Switzerland) (2019) 1615, https://doi.org/10.3390/w11081615.
[14] F.J. Wambura, O. Dietrich, G. Lischeid, Improving a distributed hydrological model using evapotranspiration-related boundary conditions as additional constraints in a data-scarce river basin, Hydrol. Process. 32 (2018) 759–775, https://doi.org/10.1002/hyp.11453.
[15] P.B. Parajuli, P. Jayakody, Y. Ouyang, Evaluation of using remote sensing evapotranspiration data in SWAT, Water Resour. Manag. 32 (2018) 985–996, https://doi.org/10.1007/s11269-017-1850-z.
[16] M.R. Herman, A.P. Nejadhashemi, M. Abouali, J.S. Hernandez-Suarez, F. Daneshvar, Z. Zhang, M.C. Anderson, A.M. Sadeghi, C.R. Hain, A. Sharifi, Evaluating the role of evapotranspiration remote sensing data in improving hydrological modeling predictability, J. Hydrol. (Amst.) 556 (2018) 39–49, https://doi.org/10.1016/j.jhydrol.2017.11.009.
[17] A. Rajib, G.R. Evenson, H.E. Golden, C.R. Lane, Hydrologic model predictability improves with spatially explicit calibration using remotely sensed evapotranspiration and biophysical parameters, J. Hydrol. (Amst.) 567 (2018) 668–683, https://doi.org/10.1016/j.jhydrol.2018.10.024.
[18] S. Lee, J. Qi, G.W. McCarty, M. Anderson, Y. Yang, X. Zhang, G.E. Moglen, D. Kwak, H. Kim, V. Lakshmi, S. Kim, Combined use of crop yield statistics and remotely sensed products for enhanced simulations of evapotranspiration within an agricultural watershed, Agric. Water Manag. 264 (2022) 107503, https://doi.org/10.1016/j.agwat.2022.107503.
[19] S. Dangol, X. Zhang, X.-Z. Liang, M. Anderson, W. Crow, S. Lee, G.E. Moglen, G.W. McCarty, Multivariate calibration of the SWAT model using remotely sensed datasets, 2023, Rem. Sens. 15 (2023) 2417, https://doi.org/10.3390/RS15092417, 2417 15.
[20] K. Beven, A manifesto for the equifinality thesis, in: J Hydrol (Amst), 2006, pp. 18–36, https://doi.org/10.1016/j.jhydrol.2005.07.007.
[21] A. Rajib, I.L. Kim, H.E. Golden, C.R. Lane, S.V. Kumar, Z. Yu, S. Jeyalakshmi, Watershed modeling with remotely sensed big data: modis leaf area index improves hydrology and water quality predictions, Rem. Sens. 12 (2020) 2148, https://doi.org/10.3390/rs12132148.
[22] J. Andersen, G. Dybkjaer, K.H. Jensen, J.C. Refsgaard, K. Rasmussen, Use of remotely sensed precipitation and leaf area index in a distributed hydrological model, J. Hydrol. (Amst.) 264 (2002) 34–50, https://doi.org/10.1016/S0022-1694(02)00046-X.
[23] S. Stisen, K.H. Jensen, I. Sandholt, D.I.F. Grimes, A remote sensing driven distributed hydrological model of the Senegal River basin, J. Hydrol. (Amst.) 354 (2008) 131–148, https://doi.org/10.1016/j.jhydrol.2008.03.006.
[24] Z. Bian, Y. Gu, J. Zhao, Y. Pan, Y. Li, C. Zeng, L. Wang, Simulation of evapotranspiration based on leaf area index, precipitation and pan evaporation: a case study of Poyang Lake watershed, China, Ecohydrol. Hydrobiol. 19 (2019) 83–92, https://doi.org/10.1016/j.ecohyd.2018.03.005.
[25] V. Gigante, V. Iacobellis, S. Manfreda, P. Milella, I. Portoghese, Influences of leaf area index estimations on water balance modeling in a mediterranean semi-arid basin, Nat. Hazards Earth Syst. Sci. 9 (2009) 979–991, https://doi.org/10.5194/nhess-9-979-2009.
[26] H. Yan, S.Q. Wang, D. Billesbach, W. Oechel, J.H. Zhang, T. Meyers, T.A. Martin, R. Matamala, D. Baldocchi, G. Bohrer, D. Dragoni, R. Scott, Global estimation of evapotranspiration using a leaf area index-based surface energy and water balance model, Remote Sens. Environ. 124 (2012) 581–595, https://doi.org/10.1016/j.rse.2012.06.004.
[27] N.L. Rane, G.K. Jayaraj, Enhancing SWAT model predictivity using multi-objective calibration: effects of integrating remotely sensed evapotranspiration and leaf area index, Int. J. Environ. Sci. Technol. 20 (2023) 6449–6468, https://doi.org/10.1007/s13762-022-04293-7.
[28] M.L. Tan, P.W. Gassman, X. Yang, J. Haywood, A review of SWAT applications, performance and future needs for simulation of hydro-climatic extremes, Adv. Water Resour. 143 (2020), https://doi.org/10.1016/J.ADVWATRES.2020.103662.
[29] L.T. Ha, W.G.M. Bastiaanssen, A. van Griensven, A.I.J.M. van Dijk, G.B. Senay, Calibration of spatially distributed hydrological processes and model parameters in SWAT using remote sensing data and an auto-calibration procedure: a case study in a Vietnamese river basin, Water (Switzerland) 10 (2018) 212, https://doi.org/10.3390/w10020212.
[30] S. Lee, W.G. McCarty, W.M. Lang, X. Li, Overview of the USDA Mid-Atlantic regional wetland conservation effects assessment project, J. Soil Water Conserv. 75 (2020) 684–694.

[31] C. Baffaut, J.M. Baker, J.A. Biederman, D.D. Bosch, E.S. Brooks, A.R. Buda, E.M. Demaria, E.H. Elias, G.N. Flerchinger, D.C. Goodrich, S.K. Hamilton, S. P. Hardegree, R.D. Harmel, D.L. Hoover, K.W. King, P.J. Kleinman, M.A. Liebig, G.W. McCarty, G.E. Moglen, T.B. Moorman, D.N. Moriasi, J. Okalebo, F. B. Pierson, E.S. Russell, N.Z. Saliendra, A.K. Saha, D.R. Smith, L.M.W. Yasarer, Comparative analysis of water budgets across the U.S. long-term agroecosystem research network, J. Hydrol. (Amst.) 588 (2020) 125021, https://doi.org/10.1016/j.jhydrol.2020.125021.

[32] S. Lee, A.M. Sadeghi, G.W. McCarty, C. Baffaut, S. Lohani, L.F. Duriancik, A. Thompson, I.-Y. Yeo, C. Wallace, Assessing the suitability of the Soil Vulnerability Index (SVI) on identifying croplands vulnerable to nitrogen loss using the SWAT model, Catena 167 (2018), https://doi.org/10.1016/j.catena.2018.04.021.

[33] S.L. Neitsch, J.G. Arnold, J.R. Kiniry, J.R. Williams, Soil & water assessment Tool theoretical documentation version 2009. https://doi.org/10.1016/j.scitotenv.2015.11.063, 2011.

[34] M.G. Wolman, Water for Maryland's Future: what We Must Do Today, 2008. Baltimore, Md.

[35] L. Sun, M.C. Anderson, F. Gao, C. Hain, J.G. Alfieri, A. Sharifi, G.W. McCarty, Y. Yang, Y. Yang, W.P. Kustas, L. McKee, Investigating water use over the Choptank River Watershed using a multisatellite data fusion approach, Water Resour. Res. 53 (2017) 5298–5319, https://doi.org/10.1002/2017WR020700.

[36] P.C. Beeson, A.M. Sadeghi, M.W. Lang, M.D. Tomer, C.S.T. Daughtry, Sediment delivery estimates in water quality models altered by resolution and source of topographic data, J. Environ. Qual. 43 (2014) 26–36, https://doi.org/10.2134/JEQ2012.0148.

[37] S. Lee, I.-Y. Yeo, A.M. Sadeghi, G.W. McCarty, W.D. Hively, M.W. Lang, Impacts of watershed characteristics and crop rotations on winter cover crop nitrate-nitrogen uptake capacity within agricultural watersheds in the Chesapeake Bay region, PLoS One 11 (2016) e0157637, https://doi.org/10.1371/journal.pone.0157637.

[38] M.C. Anderson, J.M. Norman, J.R. Mecikalski, J.A. Otkin, W.P. Kustas, A climatological study of evapotranspiration and moisture stress across the continental United States based on thermal remote sensing: 1. Model formulation, J. Geophys. Res. Atmos. 112 (2007) D10117, https://doi.org/10.1029/2006JD007506.

[39] M.C. Anderson, J.M. Norman, J.R. Mecikalski, R.D. Torn, W.P. Kustas, J.B. Basara, A multiscale remote sensing model for disaggregating regional fluxes to micrometeorological scales, J. Hydrometeorol. 5 (2004) 343–363, https://doi.org/10.1175/1525-7541(2004)005<0343:AMRSMF>2.0.CO;2.

[40] J.M. Norman, W.P. Kustas, K.S. Humes, Source approach for estimating soil and vegetation energy fluxes in observations of directional radiometric surface temperature, Agric. For. Meteorol. 77 (1995) 263–293, https://doi.org/10.1016/0168-1923(95)02265-Y.

[41] M. Anderson, F. Gao, K. Knipper, C. Hain, W. Dulaney, D. Baldocchi, E. Eichelmann, K. Hemes, Y. Yang, J. Medellin-Azuara, W. Kustas, Field-scale assessment of land and water use change over the California delta using remote sensing, Rem. Sens. 10 (2018) 889, https://doi.org/10.3390/rs10060889.

[42] F. Gao, M. Anderson, C. Daughtry, A. Karnieli, D. Hively, W. Kustas, A within-season approach for detecting early growth stages in corn and soybean using high temporal and spatial resolution imagery, Remote Sens. Environ. 242 (2020) 111752, https://doi.org/10.1016/j.rse.2020.111752.

[43] D.N. Moriasi, J.G. Arnold, M.W. Van Liew, R.L. Bingner, R.D. Harmel, T.L. Veith, Model evaluation guidelines for systematic quantification of accuracy in watershed simulations, Trans. ASABE (Am. Soc. Agric. Biol. Eng.) 50 (2007) 885–900, https://doi.org/10.13031/2013.23153.

[44] Q. Yang, X. Zhang, Improving SWAT for simulating water and carbon fluxes of forest ecosystems, Sci. Total Environ. 569–570 (2016) 1478–1488, https://doi.org/10.1016/j.scitotenv.2016.06.238.

[45] T. Hallouin, HydroEval: Streamflow Simulations Evaluator, 2020, Version 0.0. 3.

[46] R. Becker, A. Koppa, S. Schulz, M. Usman, T. aus der Beek, C. Schüth, Spatially distributed model calibration of a highly managed hydrological system using remote sensing-derived ET data, J. Hydrol. (Amst.) 577 (2019) 123944, https://doi.org/10.1016/j.jhydrol.2019.123944.

[47] T. Poméon, B. Diekkrüger, A. Springer, J. Kusche, A. Eicker, Multi-objective validation of SWAT for sparsely-gaugedWest African river basins - a remote sensing approach, Water (Switzerland) 10 (2018) 451, https://doi.org/10.3390/w10040451.

[48] K. Khalid, M.F. Ali, N.F.A. Rahman, M.R. Mispan, S.H. Haron, Z. Othman, M.F. Bachok, Sensitivity analysis in watershed model using SUFI-2 algorithm, Procedia Eng. 162 (2016) 441–447, https://doi.org/10.1016/j.proeng.2016.11.086.

[49] Y. Her, I. Chaubey, Impact of the numbers of observations and calibration parameters on equifinality, model performance, and output and parameter uncertainty, Hydrol. Process. 29 (2015) 4220–4237, https://doi.org/10.1002/hyp.10487.

[50] Y. Chen, G.W. Marek, T.H. Marek, D.K. Brauer, R. Srinivasan, Assessing the efficacy of the SWAT auto-irrigation function to simulate irrigation, evapotranspiration, and crop response to management strategies of the Texas high plains, Water (Switzerland) 9 (2017) 509, https://doi.org/10.3390/w9070509.

[51] S. Lee, I.Y. Yeo, M.W. Lang, A.M. Sadeghi, G.W. McCarty, G.E. Moglen, G.R. Evenson, Assessing the cumulative impacts of geographically isolated wetlands on watershed hydrology using the SWAT model coupled with improved wetland modules, J. Environ. Manag. 223 (2018) 37–48, https://doi.org/10.1016/j.jenvman.2018.06.006.

[52] T.R. Fisher, T.E. Jordan, K.W. Staver, A.B. Gustafson, A.I. Koskelo, R.J. Fox, A.J. Sutton, T. Kana, K.A. Beckert, J.P. Stone, G. McCarty, M. Lang, The choptank basin in transition: intensifying agriculture, slow urbanization, and estuarine eutrophication, in: Coastal Lagoons: Critical Habitats of Environmental Change, 2010, https://doi.org/10.1201/EBK1420088304.

[53] C.R. Hain, W.T. Crow, M.C. Anderson, M. Tugrul Yilmaz, Diagnosing neglected soil moisture source-sink processes via a thermal infrared-based two-source energy balance model, J. Hydrometeorol. 16 (2015) 1070–1086, https://doi.org/10.1175/JHM-D-14-0017.1.

[54] S. Lee, G.W. McCarty, G.E. Moglen, M.W. Lang, C. Nathan Jones, M. Palmer, I.-Y. Yeo, M. Anderson, A.M. Sadeghi, M.C. Rabenhorst, Seasonal drivers of geographically isolated wetland hydrology in a low-gradient, Coastal Plain landscape, J. Hydrol. (Amst.) 583 (2020) 124608, https://doi.org/10.1016/j.jhydrol.2020.124608.

[55] S. Miguel López-Ramírez, A. Mayer, L. Sáenz, E. Muñoz-Villers, F. Holwerda, N. Looker, C. Schürz, Z. Carter Berry, R. Manson, H. Asbjornsen, R. Kolka, D. Geissert, C. Lezama, A comprehensive calibration and validation of SWAT-T using local datasets, evapotranspiration and streamflow in a tropical montane cloud forest area with permeable substrate in central Veracruz, Mexico, J. Hydrol. (Amst.) 603 (2021) 126781, https://doi.org/10.1016/j.jhydrol.2021.126781.

[56] W.D. Hively, S. Lee, A.M. Sadeghi, G.W. McCarty, B.T. Lamb, A. Soroka, J. Keppler, I.Y. Yeo, G.E. Moglen, Estimating the effect of winter cover crops on nitrogen leaching using cost-share enrollment data, satellite remote sensing, and Soil and Water Assessment Tool (SWAT) modeling, J. Soil Water Conserv. 75 (2020) 362–375, https://doi.org/10.2489/JSWC.75.3.362.

[57] D. Parr, G. Wang, D. Bjerklie, Integrating remote sensing data on evapotranspiration and leaf area index with hydrological modeling: impacts on model performance and future predictions, J. Hydrometeorol. 16 (2015) 2086–2100, https://doi.org/10.1175/JHM-D-15-0009.1.

[58] D. Jiang, K. Wang, The role of satellite-based remote sensing in improving simulated streamflow: a review, Water (Switzerland) (2019) 1615, https://doi.org/10.3390/w11081615.

[59] A. Rajib, V. Merwade, Z. Yu, Rationale and efficacy of assimilating remotely sensed potential evapotranspiration for reduced uncertainty of hydrologic models, Water Resour. Res. 54 (2018) 4615–4637, https://doi.org/10.1029/2017WR021147.

[60] A. Rajib, I.L. Kim, H.E. Golden, C.R. Lane, S.v. Kumar, Z. Yu, S. Jeyalakshmi, Watershed modeling with remotely sensed big data: modis leaf area index improves hydrology and water quality predictions, Rem. Sens. 12 (2020) 2148, https://doi.org/10.3390/rs12132148.

[61] C. Albergel, S. Munier, D. Jennifer Leroux, H. Dewaele, D. Fairbairn, A. Lavinia Barbu, E. Gelati, W. Dorigo, S. Faroux, C. Meurey, P. Le Moigne, B. Decharme, J. F. Mahfouf, J.C. Calvet, Sequential assimilation of satellite-derived vegetation and soil moisture products using SURFEX-v8.0: LDAS-Monde assessment over the Euro-Mediterranean area, Geosci. Model Dev. (GMD) 10 (2017) 3889–3912, https://doi.org/10.5194/gmd-10-3889-2017.

[62] A.V.M. Ines, N.N. Das, J.W. Hansen, E.G. Njoku, Assimilation of remotely sensed soil moisture and vegetation with a crop simulation model for maize yield prediction, Remote Sens. Environ. 138 (2013) 149–164, https://doi.org/10.1016/j.rse.2013.07.018.

[63] S. Lee, G.W. McCarty, G.E. Moglen, X. Li, C.W. Wallace, Assessing the effectiveness of riparian buffers for reducing organic nitrogen loads in the Coastal Plain of the Chesapeake Bay watershed using a watershed model, J. Hydrol. (Amst.) 585 (2020) 124779, https://doi.org/10.1016/J.JHYDROL.2020.124779.

[64] S. Lee, J. Qi, G.W. McCarty, I.Y. Yeo, X. Zhang, G.E. Moglen, L. Du, Uncertainty assessment of multi-parameter, multi-GCM, and multi-RCP simulations for streamflow and non-floodplain wetland (NFW) water storage, J. Hydrol. (Amst.) 600 (2021) 126564, https://doi.org/10.1016/J.JHYDROL.2021.126564.

[65] Y. Her, S.H. Yoo, J. Cho, S. Hwang, J. Jeong, C. Seong, Uncertainty in hydrological analysis of climate change: multi-parameter vs. multi-GCM ensemble predictions, Sci. Rep. 9 (2019) 4974, https://doi.org/10.1038/s41598-019-41334-7.

[66] L. Thanh Ha, W.G. M Bastiaanssen, A. van Griensven, A.I. J M van Dijk, G.B. Senay, Calibration of spatially distributed hydrological processes and model parameters in SWAT using remote sensing data and an auto-calibration procedure: a case study in a Vietnamese river basin. https://doi.org/10.3390/w10020212, 2018.
[67] H. Haas, L. Kalin, P. Srivastava, Improved forest dynamics leads to better hydrological predictions in watershed modeling, Sci. Total Environ. 821 (2022) 153180, https://doi.org/10.1016/j.scitotenv.2022.153180.
[68] J. Ding, Q. Zhu, The accuracy of multisource evapotranspiration products and their applicability in streamflow simulation over a large catchment of Southern China, J Hydrol Reg Stud 41 (2022) 101092, https://doi.org/10.1016/j.ejrh.2022.101092.
[69] R.W. Vervoort, S.F. Miechels, F.F. van Ogtrop, J.H.A. Guillaume, Remotely sensed evapotranspiration to calibrate a lumped conceptual model: pitfalls and opportunities, J. Hydrol. (Amst.) 519 (2014) 3223–3236, https://doi.org/10.1016/j.jhydrol.2014.10.034.
[70] F. Zhao, Y. Wu, L. Wang, S. Liu, X. Wei, J. Xiao, L. Qiu, P. Sun, Multi-environmental impacts of biofuel production in the U.S. Corn Belt: a coupled hydro-biogeochemical modeling approach, J. Clean. Prod. 251 (2020) 119561, https://doi.org/10.1016/j.jclepro.2019.119561.
[71] M. Basso, D.C.S. Vieira, T.B. Ramos, M. Mateus, Assessing the adequacy of SWAT model to simulate postfire effects on the watershed hydrological regime and water quality, Land Degrad. Dev. 31 (2020) 619–631, https://doi.org/10.1002/ldr.3476.
[72] F. Dosdogru, L. Kalin, R. Wang, H. Yen, Potential impacts of land use/cover and climate changes on ecologically relevant flows, J. Hydrol. (Amst.) 584 (2020) 124654, https://doi.org/10.1016/j.jhydrol.2020.124654.